Available on the CERN CDS information server **CMS PAS SUS-11-008**

CMS Physics Analysis Summary

Contact: cms-pag-conveners-susy@cern.ch

2011/12/04

Search for supersymmetry with the razor variables

The CMS Collaboration

Abstract

A search is performed for heavy particle pairs produced in $\sqrt{s} = 7$ TeV proton-proton collisions with ~ 800 pb^{-1} of data collected by the CMS experiment in 2011 at the CERN Large Hadron Collider. The search is sensitive to generic supersymmetry models provided superpartner particles are kinematically accessible, with minimal assumptions on properties of the lightest superpartner particle. The kinematic consistency of the selected events is tested against the hypothesis of heavy particle pair production using the dimensionless *razor* variable R, related to the missing transverse energy E_T^{miss}. The new physics signal is characterized by a broad peak in the distribution of M_R, an event-by-event indicator of the heavy particle mass scale. After background modeling based on data no significant deviation is observed from the Standard Model expectation. The results are interpreted in the context of the Constrained Minimal Supersymmetric Standard Model.

1 Introduction

Several theoretical frameworks have been proposed that predict heavy partners of Standard Model (SM) particles, including a weakly-interacting massive particle that serves as a viable candidate for dark matter. The stability of the dark matter particle is guaranteed by a conserved quantum number, for example, R-parity in models of supersymmetry (SUSY), Kaluza-Klein parity in models of universal extra dimensions (UED), and T-parity in some models of Little Higgs. This conserved quantum number also ensures that most or all of the heavier partner particles are produced in pairs. Thus the generic signal for new physics in these frameworks is pair production of heavy particles and a final state characterized by two weakly-interacting massive objects. Experimental searches for SUSY at hadron colliders have focused on squark and gluino pair production into final states with multiple energetic hadronic jets and/or leptons, combined with large missing transverse energy (E_T^{miss}) from the two lightest superpartners (LSPs) produced in the decay chains.

The focal point for the *razor* analysis [1, 2] is the production of pairs of heavy particles (of which squarks and gluinos are examples), whose masses are significantly larger than those of any SM particle. The analysis is designed to kinematically discriminate the pair production of heavy particles from SM backgrounds, without making strong assumptions about the E_T^{miss} spectrum or any details of the decay chains of these particles. The baseline selection requires two or more reconstructed objects, which can be any combination of calorimetric jets, isolated electrons or muons. These objects are grouped into two *megajets*. The razor analysis tests the consistency, event by event, of the hypothesis that the two megajets represent the visible portion of the decays of two heavy particles. This test uses two kinematic variables, one of which is an estimator of the parent particle mass scale, while the other is a ratio related to the E_T^{miss} fraction and transversality of the event.

Standard Model events can have significant E_T^{miss} from energetic neutrinos, or exhibit fake E_T^{miss} due to mismeasurements, detector noise, or problems in reconstruction. These SM backgrounds are strongly suppressed by simple selections in the razor kinematic variables. Equally important, the remnant of the SM background is well-modeled by simple exponential distributions in the two-dimensional plane defined by the razor variables. This strategy is complementary to traditional searches for signals in the tails of the E_T^{miss} distribution [3–10], and is here applied in 1 fb $^{-1}$ of data collected with the Compact Muon Solenoid (CMS) detector.

2 The CMS Apparatus

A description of the CMS detector can be found elsewhere [11]. A characteristic feature of the CMS detector is its superconducting solenoid magnet, of 6 m internal diameter, providing a field of 3.8 T. The silicon pixel and strip tracker, the crystal electromagnetic calorimeter (ECAL) and the brass/scintillator hadron calorimeter (HCAL) are contained within the solenoid. Muons are detected in gas-ionization chambers embedded in the steel return yoke. The ECAL has an energy resolution of better than 0.5 % above 100 GeV. The HCAL combined with the ECAL, measures the jet energy with a resolution $\Delta E/E \approx 100\,\%/\sqrt{E/\,\mathrm{GeV}} \oplus 5\,\%$.

CMS uses a coordinate system with the origin located at the nominal collision point, the x-axis pointing towards the center of the LHC, the y-axis pointing up (perpendicular to the LHC plane), and the z-axis along the counterclockwise beam direction. The azimuthal angle ϕ is measured with respect to the x-axis in the xy plane and the polar angle θ is defined with respect to the z-axis. The pseudorapidity is $\eta = -\ln[\tan(\theta/2)]$.

3 The Razor Analysis

The razor kinematics is based on the generic process of the pair production of two heavy particles, each decaying to an unseen particle plus jets. This includes SUSY signals with complicated and varied decay chains, or the simplest case of a pair of squarks each decaying to a quark and an LSP. All such processes are treated on an equal footing by forcing every event into a dijet topology; this is done by combining all jets in the event into two megajets. When an isolated lepton is present, it can be included in the megajets or not as explained in [2]. For the 1 fb^{-1} analysis the trigger requirements, pileup conditions, and pile-up subtraction dictate that isolated electrons enter the megajet reconstruction as jets, while isolated muons are not included in the megajet reconstruction and mimic the contributions of neutrinos. The megajet reconstruction is thus based on a calorimeter-driven view of the events.

To the extent that the pair of megajets accurately reconstruct the visible portion of the underlying parent particle decays, the signal kinematics is equivalent to pair production of heavy squarks $\tilde{q}_1$, $\tilde{q}_2$, with $\tilde{q}_i \to \text{j}_i\tilde{\chi}_i$, where the $\tilde{\chi}_i$ are LSPs and j_i denotes the visible products of the decays. For simplicity we will use the approximation that the j_i are massless.

The standard computation of the cross section for such a process uses a parameterization of the phase space and the matrix element extracted from consideration of three preferred reference frames: the rest frames of the two squarks and the center of mass (CM) frame.

In the rest frame of the *i*th squark, the 4-momenta of the squark and its decay products have the simple form

$$\begin{aligned} p_{\tilde{q}_i} &= M_{\tilde{q}}(1,0)\;, && (1)\\ p_{\text{j}_i} &= \frac{M_\Delta}{2}(1,\hat{u}_i)\;, && (2)\\ p_{\chi_i} &= \frac{M_\Delta}{2}(\frac{1}{\beta_\Delta},-\hat{u}_i)\;, && (3) \end{aligned}$$

where the $\hat{u}_i$ are unit vectors in the directions of the visible decay products,

$$M_\Delta \equiv \frac{M_{\tilde{q}}^2 - M_{\tilde{\chi}}^2}{M_{\tilde{q}}} = 2M_{\tilde{\chi}}\gamma_\Delta\beta_\Delta\;, \qquad (4)$$

and β_Δ is the boost parameter to the rest frame of the LSP $\tilde{\chi}_i$. The other preferred frame is the $\tilde{q}_1\tilde{q}_2$ CM frame, with

$$\begin{aligned} p_{\tilde{q}_1} &= \gamma_{CM}M_{\tilde{q}}\,(1,\;\beta_{CM}\hat{u}_{\tilde{q}})\;, && (5)\\ p_{\tilde{q}_2} &= \gamma_{CM}M_{\tilde{q}}\,(1,-\beta_{CM}\hat{u}_{\tilde{q}})\;, && (6) \end{aligned}$$

where $\hat{u}_{\tilde{q}}$ is a unit vector in the direction of the first squark, and β_{CM} is the boost parameter from the CM frame to the $\tilde{q}_1$ rest frame. In the CM frame the energies of the visible decay products can be written

$$\begin{aligned} E_{\text{j}_1} &= \frac{\gamma_{CM}M_\Delta}{2}(1+\beta_{CM}\hat{u}_{\tilde{q}}\cdot\hat{u}_1)\;, && (7)\\ E_{\text{j}_2} &= \frac{\gamma_{CM}M_\Delta}{2}(1+\beta_{CM}\hat{u}_{\tilde{q}}\cdot\hat{u}_2)\;. && (8) \end{aligned}$$

Since the second term typically averages to zero, the energy distribution for the visible decay products as measured in the CM frame peaks around $(\gamma_{CM} M_\Delta)/2$.

The problem with the conventional parameterization of this process is that, with two unseen LSPs, there are not enough experimental observables to reconstruct any of the three reference frames just described. This is true even in the absence of initial state p_T (as will now be assumed throughout), where the CM frame is just a longitudinal boost from the lab frame.

The strategy of the razor analysis is to approximate these unknown frames with a razor frame that is defined unambiguously from measured quantities in the lab frame. Event by event, razor frame observables then estimate the scales M_Δ and $\gamma_{CM} M_\Delta$ seen above.

A razor frame is defined by finding a longitudinal boost from the lab frame to a frame where the visible energies can be written in terms of an overall scale that is manifestly invariant under longitudinal boosts. This then defines a razor frame where the scale of the visible energies is set by a quantity that should approximate $\gamma_{CM} M_\Delta$ in the (unknown) CM frame. The longitudinal boost used here is defined as:

$$\beta_L^{R^*} \equiv \frac{p_z^{\mathrm{j}_1} + p_z^{\mathrm{j}_2}}{E_{\mathrm{j}_1} + E_{\mathrm{j}_2}} . \tag{9}$$

The razor boost $\beta_L^R *$ defines a frame where the visible four-momenta reduce to

$$p_{\mathrm{j}_1} = (\frac{1}{2}(M_R - \frac{(\vec{p}_T^{\,\mathrm{j}_1} - \vec{p}_T^{\,\mathrm{j}_2}) \cdot \vec{E}_T^{miss}}{M_R}), p_T^{\mathrm{j}_1}, p_z) , \tag{10}$$

$$p_{\mathrm{j}_2} = (\frac{1}{2}(M_R + \frac{(\vec{p}_T^{\,\mathrm{j}_1} - \vec{p}_T^{\,\mathrm{j}_2}) \cdot \vec{E}_T^{miss}}{M_R}), p_T^{\mathrm{j}_2}, -p_z) , \tag{11}$$

where M_R is the longitudinal boost invariant

$$M_R \equiv \sqrt{(E_{\mathrm{j}_1} + E_{\mathrm{j}_2})^2 - (p_z^{\mathrm{j}_1} + p_z^{\mathrm{j}_2})^2} , \tag{12}$$

and the longitudinal momentum p_z is determined from the massless on-shell conditions. Obviously the R^* this frame always exists since the magnitude of $\beta_L^{R^*}$ is less than unity. This definition of M_R is enhanced w.r.t. [2] to avoid configurations where M_R is ill-defined due to unphysical Lorentz transformations. Here M_R as defined by (12) is an estimator of $\gamma_{CM} M_\Delta$.

The next step of the razor strategy is to define a transverse observable that can also serve as an event-by-event estimator of the underlying scale M_Δ. As usual for transverse quantities we expect M_Δ to be related to a kinematic edge rather than a peak.

Several choices of the transverse observable are plausible. To the extent that events match the assumed topology, the maximum value of the scalar sum of the megajets transverse momenta (p_T^1, p_T^2) is M_Δ. The maximum value of the E_T^{miss} is also M_Δ. Especially useful is M_T^R, a kind of average transverse mass whose maximum value for signal events is also M_Δ:

$$M_T^R \equiv \sqrt{\frac{E_T^{miss}(p_T^{j1} + p_T^{j2}) - \vec{E}_T^{miss} \cdot (\vec{p}_T^{\,j1} + \vec{p}_T^{\,j2})}{2}} . \tag{13}$$

Given a global estimator M_R and a transverse estimator M_T^R, the razor dimensionless ratio is defined as

$$R \equiv \frac{M_T^R}{M_R} . \tag{14}$$

Signal events are characterized by the heavy scale M_Δ, while backgrounds are not. Qualitatively we expect M_R to peak for the signal over a steeply falling background. Thus the search for an excess of signal events in a tail of a distribution is recast as a search for a peak on top of a steeply falling Standard Model residual tail.

To extract the peaking signal we need first to reduce the QCD multijet background to manageable levels. This is achieved by imposing a threshold value for R. Recall that for signal events M_T^R has a maximum value of M_Δ (i.e. a kinematic edge); thus R has a maximum value of approximately 1 and the distribution of R for signal peaks around 0.5, in contrast to QCD multijet events which peak at zero. These properties motivate the appropriate kinematic requirements for the signal selection and background reduction. We note that, while M_T^R and M_R measure the same scale (one as an end-point the other as a peak), they are largely uncorrelated for signal events as shown in Fig. 1.

4 Analysis path

In both simulation and data, the distributions of SM background events are seen to have a simple exponential dependence on the razor variables R and M_R over a large fraction of the R^2-M_R plane. The analysis uses simulated events to understand the shapes of the SM background distributions, the number of independent parameters needed to describe them, and extract initial estimates of the values of these parameters. For each of the main SM backgrounds, a control sample is then defined from a subset of the data that is dominated by this particular background in order to obtain a data-driven description of the shapes of the background components. A full SM background representation is thus built using statistically independent data samples; this is used as input for a global fit to the remaining data. The fit is performed in the corner of low M_R and small R^2; the distribution is then extrapolated on an orthogonal region of the R^2-M_R plane, defined such that the two regions overlap when projected on either one of the axes (R^2 or M_R). The fit includes parameters describing the shapes of the R^2-M_R distributions of the SM backgrounds as well as the relative fraction of each background.

The main steps in the analysis path are as follows:

1. Inclusive data sets are collected with the electron, muon, and hadronic jet CMS triggers, multiobject triggers, and the suite of razor triggers introduced in the CMS high level trigger menu in the spring of 2011. We refer to the 2011 data collected prior to the deployment of the razor triggers and corresponding to integrated luminosity of $\sim$300 pb^{-1} as NR11. We refer to the 2011 data collected with the razor triggers and corresponding to integrated luminosity of $\sim$800 pb^{-1} as YR11. The YR11 data is used for the search, while the NR11 data provides control samples that determine the initial values used in fits to YR11 data, and establishes the consistency of the $R^2 - M_R$ shape parameterizations used in those fits.

2. These data sets are examined for the presence of a well-identified isolated electron or muon. Based on the presence or absence of such a lepton, the event is moved to one of the 6 disjoint event samples referred to as the electron (ELE), muon (MU), hadronic (HAD) and dilepton (MU-MU, ELE-ELE, MU-ELE) *boxes*. The dilepton boxes are hierarchical with the muon having priority over the electron (for example an $ee\mu$ event will go in the MU-ELE box and not in the ELE-ELE); the details are shown in Fig. 2. This hierarchy corresponds to an ordering of event samples from those with the least background population to those with the most. Each of the 5 lepton boxes is further sub-divided according to the presence or absence of a b-tagged jet.

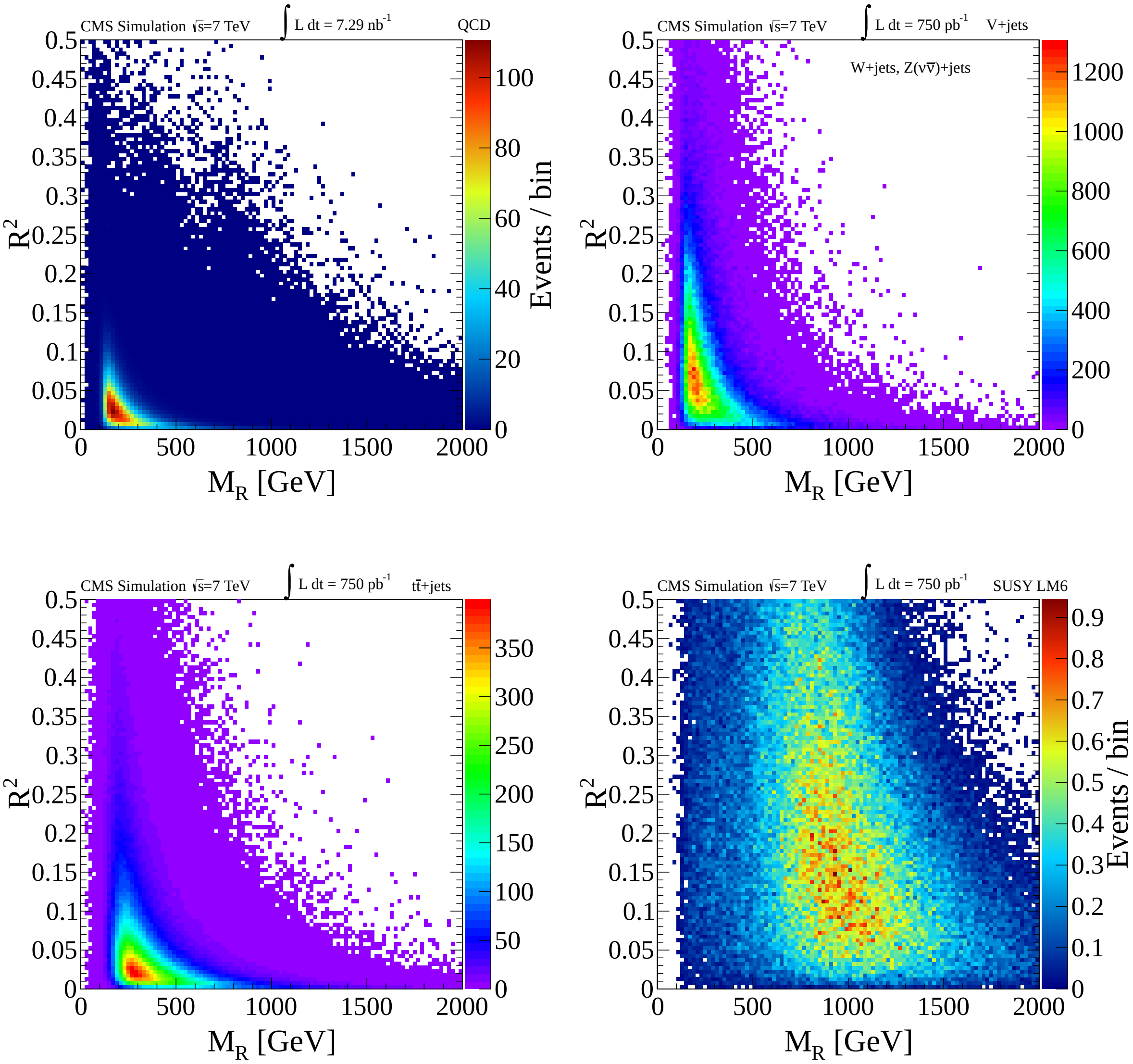

Figure 1: Scatter plot in the (M_R, R^2) plane for simulated events: (top left) QCD multijet, (top right) W+jets and $Z(\nu\bar{\nu}$+jets, (bottom left) $t\bar{t}$+jets, and (bottom right) the SUSY benchmark model LM6 [12] with $M_\Delta = 831$ GeV. The yields are normalized to an integrated luminosity of $\sim$ 800 pb^{-1}, except in the QCD multijet case where we use the corresponding generated luminosity. The bin size is (20 GeV $\times$ 0.005).

3. Three additional event samples are introduced to serve as data control samples for the QCD multijet background in the HAD, ELE, and MU boxes. The QCD multijet control sample for the HAD box is obtained from event samples recorded with pre-scaled jet triggers, while the QCD multijet control samples for the ELE and MU boxes are obtained by inverting the lepton isolation requirement.

4. Simulated samples are produced for the major SM backgrounds: QCD multijets, W+jets, Z+jets, and $t\bar{t}$, in all of the boxes. The simulated samples are used to find the regions of the R^2-M_R plane in each box where the backgrounds can be described by simple exponentials. The parameters describing these exponential shapes in the simulated samples

are extracted for each box and for each SM background, to be used as initial values in the fits to data control samples.

5. Data control samples are defined in the NR11 data dominated by $t\bar{t}$, Z+jets, and W+jets. For each box we obtain a top-enriched sample by requiring at least one b-tagged jet; simulated samples indicate that the shape of the R^2-M_R distributions are not biased by the b-tag requirement. The Z+jets enriched sample is the sum of the portions of the MU-MU and ELE-ELE boxes not containing a b-tag and and with dilepton invariant mass in the window between 60 and 120 GeV. The W+jets dominated sample is taken as the portions of the 5 lepton boxes not included in the $t\bar{t}$-dominated or Z+jets-dominated samples.

6. The R^2-M_R shape parameters are extracted from each data control sample, performing 2D maximum likelihood (ML) fits for each of the relevant boxes that define the sample. Hence we obtain a preliminary description of the Standard Model background shapes, component by component.

   These samples provide initial values and constraints for the global fit of the background shape in the R^2-M_R sideband, implemented by multiplying the likelihood by Gaussian penalty terms centered around these initial values.

7. Using as input the SM representation built with the NR11 data, a 2D ML fit is performed for the YR11 data in R^2-M_R sideband fit regions of the HAD, ELE, and MU boxes as well as the dilepton boxes. The yield of each SM background component is floated.

   For the HAD box, the $Z \rightarrow \nu\bar{\nu}$+jets (W+jets) background shape is floated around the expected distribution estimated from the fit results on the data for W+jets in the MU (ELE) box. Results from similar fits to Monte Carlo simulated events demonstrate that these shapes are consistent within the available precision.

8. The fits to the sideband regions return the yield and shape for each background. Using this background description we obtain a simultaneous prediction for the background yield in defined signal regions in the R^2-M_R plane for a given box. The uncertainty on the fit parameters and the correlation among them (as described by the covariance matrix returned by the fits) are taken into account. The expected and observed yields are compared in each signal region.

9. Observing no significant excess we proceed to set limits using a hybrid CL_s [13] test on the full R^2-M_R plane.

Each of these steps is described in more detail later.

5 Monte Carlo Event Samples

The design of the analysis was guided by studies of Monte Carlo event samples generated with the PYTHIA6 [14] and MADGRAPH V4.22 [15] programs, simulated using the CMS GEANT-based [16] detector simulation, and then processed by the same software used to reconstruct real collision data. Events with QCD multijets, top quarks and electroweak bosons where generated with MADGRAPH interfaced with PYTHIA for parton showering, hadronization and the underlying event description. To generate Monte Carlo samples for SUSY the mass spectrum was first calculated with SOFTSUSY [17] and the decays with SUSYHIT [18]. The PYTHIA program was used with the SLHA interface [19] to generate the events. The generator level cross section and the k-factors for the Next-to-Leading Order (NLO) cross section calculation were computed using PROSPINO [20].

6 Event Selection

The analyses uses a set of dedicated triggers, which apply lower thresholds on the values of R and M_R, computed online from the reconstructed jets and missing energy. Three trigger categories are used: i) hadronic triggers, applying moderate/tight requirements on R and M_R to events with two jets of $p_T > 56$ GeV; ii) muon triggers, similar to the hadronic triggers, but with looser requirements on R and M_R and of at least one muon in the central part of the detector with $p_T > 10$ GeV iii) electron triggers, with similar R and M_R requirements and at least one electron of p_T >10 GeV, satisfying loose isolation criteria. All of these triggers are fully efficient in the kinematic regions used for this analysis.

In addition, a set of pre-scaled and unprescaled triggers is used to define the control samples for the NR11 dataset, for which the dedicated razor triggers were not available.

Events are required to have at least one good reconstructed interaction vertex [21]. When multiple vertices are found, the one with the highest associated $\sum_{track} p_T^2$ is used. Jets are reconstructed offline from calorimeter energy deposits using the infrared-safe anti-k_T [22] algorithm with radius parameter 0.5. Jets are corrected for the non-uniformity of the calorimeter response in energy and η using Monte Carlo and data derived corrections and are required to have $p_T > 60$ GeV and $|\eta| < 3.0$.

The jet energy scale uncertainty for these corrected jets is 5% [23]. The E_T^{miss} is reconstructed using the particle flow algorithm [24].

Muons in CMS are reconstructed as either *StandAloneMuons* (track in the muon detector with low momentum resolution), *GlobalMuons* (outside-in approach seeded by a *StandAloneMuon* with a global fit using hits in the muon, silicon strip and pixel detectors) and *TrackerMuons* (inside-out approach seeded by an offline silicon strip track, using the muon detector only for muon identification without refitting the track). Most good quality muons are reconstructed as all three types at the same time, and the momentum resolution is dominated by the inner tracker system up to about 200 GeV in transverse momentum. We require the muon to be reconstructed as *GlobalMuon*, with $\chi^2/\mathrm{ndof} < 10$ on the global fit, having at least one good muon hit, or a *TrackerMuon*, provided it has one pixel hit and hits in at least two muon stations.

Two muon category selections are used with $p_T > 10$ GeV; these *tight* and *loose* working points use a cut-based approach. Except for the isolation requirement, these are similar to the muon selection criteria used for the measurement of the inclusive W and Z cross sections [25], as follows:

- more than 10 hits in the inner tracker;
- pseudorapidity $|\eta|$ must be smaller than 2.1; calculated with respect to the primary vertex;

In addition the tight muons satisfy an isolation requirement based on summing the p_T of tracks and the energies of calorimetric energy deposits in a ΔR ¡ 0.3 cone in η-ϕ, an impact parameter requirement in the transverse plane $|d_0| < 0.2$ cm and a requirement of at least one pixel hit.

We select electrons using a cut-based approach similar to the electron selection criteria used for the measurement of the inclusive W and Z cross sections [25] for working points WP80, WP95. The specific requirements to select prompt electrons are the following:

- Basic acceptance cuts $p_T > 20$ GeV/c and $|\eta| < 2.5$;
- Standard electron identification is applied to barrel (endcap) electrons as follows:

- The lateral shower shape, $\sigma_{i\eta i\eta} < 0.01$ (0.03)
- The track-cluster matching in the ϕ-direction, $\Delta\phi_{\text{in}} < 0.06$ (0.03)
- The track-cluster matching in the η-direction, $\Delta\eta_{\text{in}} < 0.004$ (0.007)

When isolation requirements are applied to the electron WP80, WP95 categories and tight muon category the combined (ECAL+HCAL+tracker) isolation is used, and is corrected for pileup (PU).

The reconstructed hadronic jets and isolated electrons, are grouped into two megajets, when at least two such objects are present in the event. Reconstructed muons are not included in the megajet grouping; the dichotomy between muons and electrons is dictated by the fact that electrons are not distinguished from jets in the trigger. The megajets are constructed as a sum of the four-momenta of their constituent objects. After considering all possible partitions of the objects into two megajets, the combination minimizing the invariant masses summed in quadrature of the resulting megajets is selected among all combinations for which the R frame is well defined.

6.1 Box Classification

After the application of the baseline selection and calculation of the variables R and M_R, the remaining events are assigned to one final state box according to the isolated lepton content of the event. Six different boxes are considered in the analysis, corresponding to zero, one and two lepton final states, split according to lepton flavor (electrons and muons). The lepton p_T thresholds in the definition of the boxes are chosen such that the lepton triggers used to select events are approximately fully-efficient. The six boxes are

- ELE-MU Box: Events must contain at least one WP80 electron with $p_T > 20$ GeV/c and at least one tight muon with $p_T > 10$ GeV/c.
- MU-MU Box: Events must contain at least two loose muons with $p_T > 15$ GeV/c and $p_T > 10$ GeV/c, respectively and at least one tight muon with $p_T > 10$ GeV/c.
- ELE-ELE Box: Events must contain a WP80 electron with $p_T > 20$ GeV/c and at least one WP95 electron with $p_T > 10$ GeV/c.
- MU Box: Events must contain at least one tight muon with $p_T > 10$ GeV/c.
- ELE Box: Events must contain at least one WP80 electron with $p_T > 20$ GeV/c.
- HAD Box: Events must not satisfy any other box requirements.

In addition, for the leptonic boxes we require $M_R > 300$ GeV and $0.09 < R^2 < 0.5$, while for the hadronic box we require $M_R > 400$ GeV and $0.16 < R^2 < 0.5$. These requirements are the loosest possible compatible with the validity of the background description and the request of a fully-efficient trigger. They identify the *full region* of the R^2-M_R plane, where the analysis is performed.

In order to prevent ambiguities when an event satisfies the selection requirements of more than one box, the boxes are arranged in a predefined hierarchy. The decision to assign an event to a given box is evaluated in a preferential order, with an event being uniquely assigned to the first box whose criteria the event satisfies. The hierarchy and box classification procedure is described in the flow-diagram of Fig. 2.

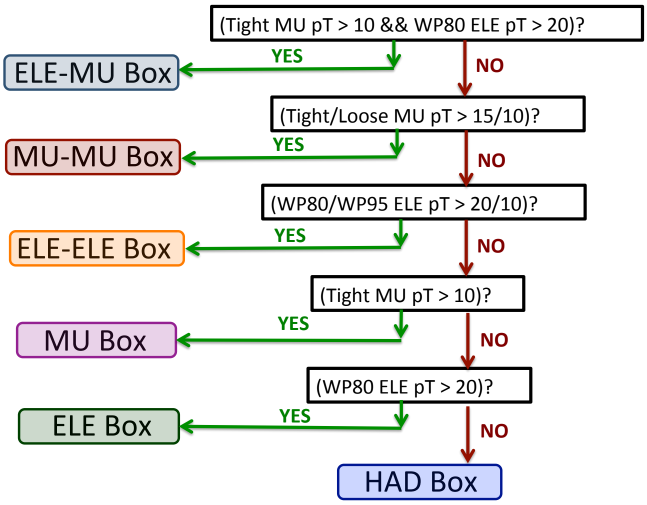

Figure 2: Flow diagram of box classification logic. The box selection proceeds according to a box hierarchy in order to ensure complete orthogonality of box selections and to resolve ambiguities when an event satisfies more than one box's selection criteria.

7 Backgrounds

In traditional searches for SUSY based on missing transverse energy, it is difficult to model the tails of the E_T^{miss} distribution, and the contribution from events with spurious instrumental effects. The QCD multijet production is an especially difficult background due to its large cross section and complicated modeling of the high p_T and E_T^{miss} tails. In this analysis a threshold on R makes it possible to remove the QCD multijet background.

Apart from the QCD multijet background, the remaining backgrounds in the lepton, dilepton and hadronic boxes are processes with genuine E_T^{miss} due to energetic neutrinos and leptons from massive vector boson decays, including W's from top quark decays and diboson production. After applying an R threshold, the M_R distributions in the single lepton, dilepton, and hadronic boxes are very similar for these backgrounds; this similarity is exploited in their modeling and normalization.

7.1 QCD multijet background

The QCD multijet control sample for the hadronic box is defined from event samples recorded with pre-scaled jet triggers and passing the baseline analysis selection for events without a well-identified isolated electron or muon. The trigger requires at least two jets with average uncorrected p_T thresholds of 60 GeV$/c$. The QCD multijet background dominates these samples for low M_R allowing the extraction of the M_R shapes with different R_{cut} thresholds for QCD multijet events.

The M_R distributions for events satisfying the QCD control box selection, for different values of the R_{cut} threshold, are shown in Fig. 3 (left). The M_R distribution is exponentially falling, after a turn-on at low M_R resulting from the p_T threshold requirement on the jets entering the megajet calculation. The exponential region of these distributions is fitted for each value of

R^2 to extract the coefficient in the exponent, denoted by S. The value of S that maximizes the likelihood in the exponential fit is found to be a linear function of R^2_{cut} as shown in Fig. 3 (right); fitting S in the form $S = a + bR^2_{\text{cut}}$ determines the values of a and b.

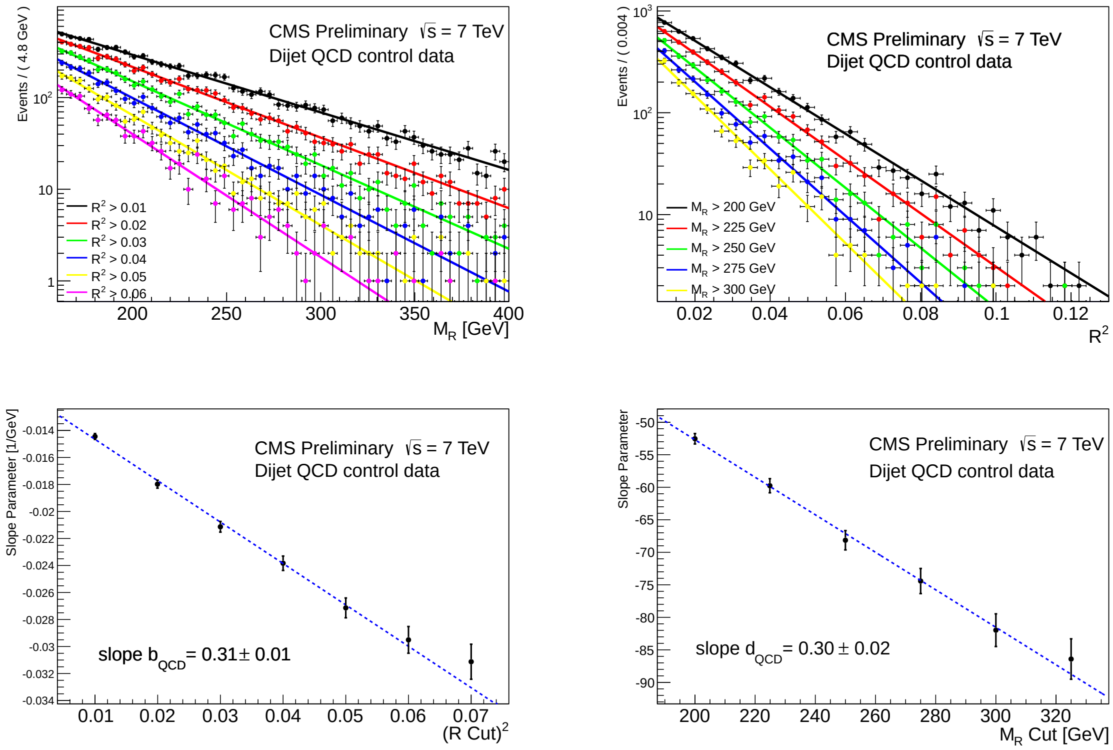

Figure 3: (Top left) M_R distributions for different values of the R^2 threshold for events in data selected in the QCD control box. (Top right) R^2 distributions for different values of the M_R threshold for events in data selected in the QCD control box. (Bottom left) The exponential slope S from fits to the M_R distribution, as a function of the square of the R^2 threshold for data events in the QCD control box. (Bottom right) The coefficient in the exponent S from fits to the R^2 distribution, as a function of the square of the M_R threshold for data events in the QCD control box.

The R^2_{cut} distributions for events satisfying the QCD control box selection, for different values of the M_R threshold, are shown in Fig. 3 (left). The R^2 distribution is exponentially falling, after a turn-on at low R^2. The exponential region of these distributions is fitted for each value of M_R^{cut} to extract the coefficient in the exponent, again denoted by S'. The value of S' that maximizes the likelihood in the exponential fit is found to be a linear function of M_R^{cut} as shown in Fig. 3 (right); fitting S' in the form $S' = c + dM_R^{\text{cut}}$ determines the values of c and d. The d slope parameter is found to equal the b slope parameter within an accuracy of a few percent as shown in Fig. 3. This is used in building a 2D probability density function (pdf) that analytically describes the R^2 vs M_R distribution and recovers an exponential distribution in $M_R(R^2)$ after integrating out $R^2(M_R)$, exploiting the equality $d = b$.

The other backgrounds exhibit the same behavior; each SM process can be described with the same functional form but different parameters.

7.2 W+jets, Z+jets and top+X backgrounds

7.2.1 MU and ELE boxes

In both simulated and data events in the muon (MU) and electron (ELE) boxes, the M_R distribution is well described with two independent exponential components. The first component of $W(\ell\nu)$+jets contains events where the electron or muon significantly contributes in the mega-jet reconstruction, and has a steeper slope compared to the second component. Both slopes along with their relative and absolute normalizations are simultaneously floated. The M_R distributions as a function of R^2 in the data are shown in Fig. 4 (top left) in the MU box with the requirement of 0 b-tagged jets. The slope parameters characterizing the exponential behavior of the 1^{st} $W(\mu\nu)$+jets and 2^{nd} components are shown in Fig. 4 (center,right). The values of $b1$ and $b2$ that describe the R^2 dependence of the slopes are in good agreement with the values extracted from simulated $W(\ell\nu)$+jets events as shown in the same figures (bottom).

The R^2 distributions as a function of M_R in the data are shown in Fig. 5 (top left) in the MU box with the requirement of 0 b-tagged jets. The slope parameters characterizing the exponential behavior of the 1^{st} $W(\mu\nu)$+jets and 2^{nd} components are shown in Fig. 5 (center,right). The values of $d1$ and $d2$ that describe the M_R dependence of the slopes are in good agreement with the values extracted from simulated $W(\ell\nu)$+jets events as shown in the same figures (bottom). Furthermore the extracted values of $d_1(d_2)$ are in agreement with the extracted values of $b_1(b_2)$.

7.2.2 Dilepton Boxes

The dilepton boxes are expected to be populated by the Z+jets candle events for the ELE-ELE, MU-MU boxes, and $t\bar{t}$ for these boxes and the MU-ELE box. In the 2010 analysis with 35 pb^{-1} these boxes were poorly populated, and the normalization of the Z+jets and $t\bar{t}$+jets backgrounds was performed using the W+jets and $t\bar{t}$+jets measured cross sections and the razor scaling in the ELE, MU boxes. In the current analysis the dilepton boxes are sufficiently populated by Z+jets candle events and $t\bar{t}$ events. The NR11 dataset collected before the deployment of the razor triggers is used to define control samples for these backgrounds.

We find the M_R distributions as a function of R^2 in the $t\bar{t}(2\ell 2\nu)$+jets MADGRAPH simulated events in the dilepton final states (ELE-ELE, MU-MU, MU-ELE) are independent of the lepton flavor combination. This background component is similar in all boxes and for its shape and normalization we use the same initial values.

8 Background Determination

We perform an extended and unbinned maximum likelihood (ML) fit, using the ROOFIT fitting tool [26]. For each box, the fit is performed in the portion of the R^2-M_R plane delimited by the green-dashed contours in Fig. 8 and Fig. 9. We refer to this region as the *fit region*. The fit provides a full description of the Standard Model background in the R^2-M_R plane in each box. The likelihood function for a given box is written as [27]:

$$\mathcal{L}_b = \frac{e^{-(\sum_{j\in SM} N_j)}}{N!}\prod_{i=1}^{N}\Big(\sum_{j\in SM} N_j P_j(M_{R,i}, R_i^2)\Big)\,, \tag{15}$$

where N is the total number of events in the box; the sum runs on all the Standard Model processes relevant for that box, N_j is the yield of a given fit sample in the box, and $P_j(M_R, R^2)$ is the two-dimensional pdf describing the R^2 versus M_R distribution of the considered process.

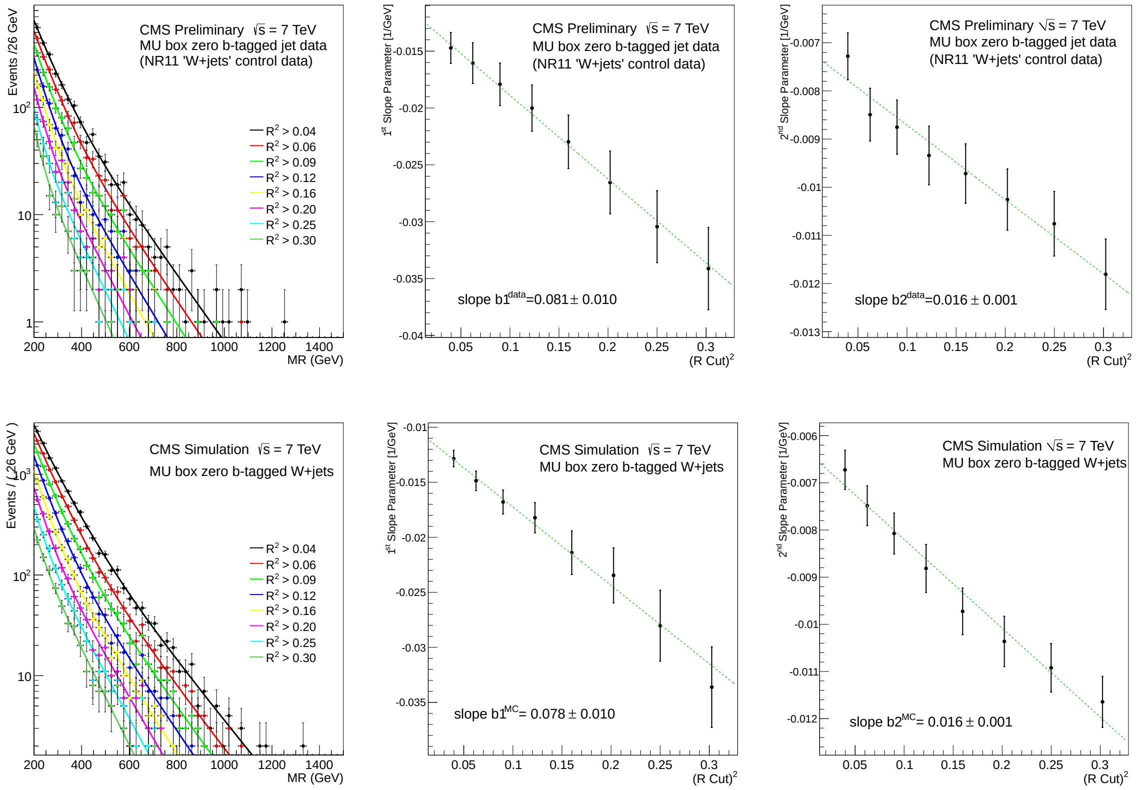

Figure 4: (Top left) M_R distributions for different values of the R^2 threshold for events in data selected in the MU box with the requirement of 0 b-tagged jets. The dotted lines show two independent exponential components fit to the the M_R distribution, (top center) value of the first exponential slope S from fits to the M_R distribution, as a function of the R^2 threshold (top right) value of the second exponential slope S from fits to the M_R distribution, as a function of the R^2 threshold. (Bottom) The corresponding in simulated W+jets events.

The P_j function is written as the sum of two instances of the same function (two *components*)

$$P_j(R^2, M_R) = (1 - f_2^j) \times F_j^{1st}(M_{R,i}, R_i^2) + f_2^j \times F_j^{2nd}(M_{R,i}, R_i^2)\,, \qquad (16)$$

where f_2^j is the relative fraction of the second component and each component is written as:

$$F_j(R^2, M_R) = \left[k_j(M_R - M_{R,j}^0)(R^2 - R_{0,j}^2) - 1\right] e^{-k_j(M_R - M_{R,j}^0)(R^2 - R_{0,j}^2)}\,. \qquad (17)$$

When integrated on M_R (R^2), this function recovers the exponential behavior on R^2 (M_R). The k_j parameters of the function are the same as the b and d parameters introduced in Section 7 that determine the scaling of the exponential constant as a function of the threshold on M_R and R^2. The identity $b = d$ is built into the functional form of Eq. 17.

While the shape of the first component is in general box dependent, the second component is found to be box independent in simulation studies as well as in fits to the NR11 data with either a b-tag requirement or a b-tag veto. This behavior is found to be associated with large initial state radiation (ISR). While the final fit does not assume a universal second component for all the pdf's corresponding to a given SM process, it outputs a universal component in the result within the accuracy of the fit.

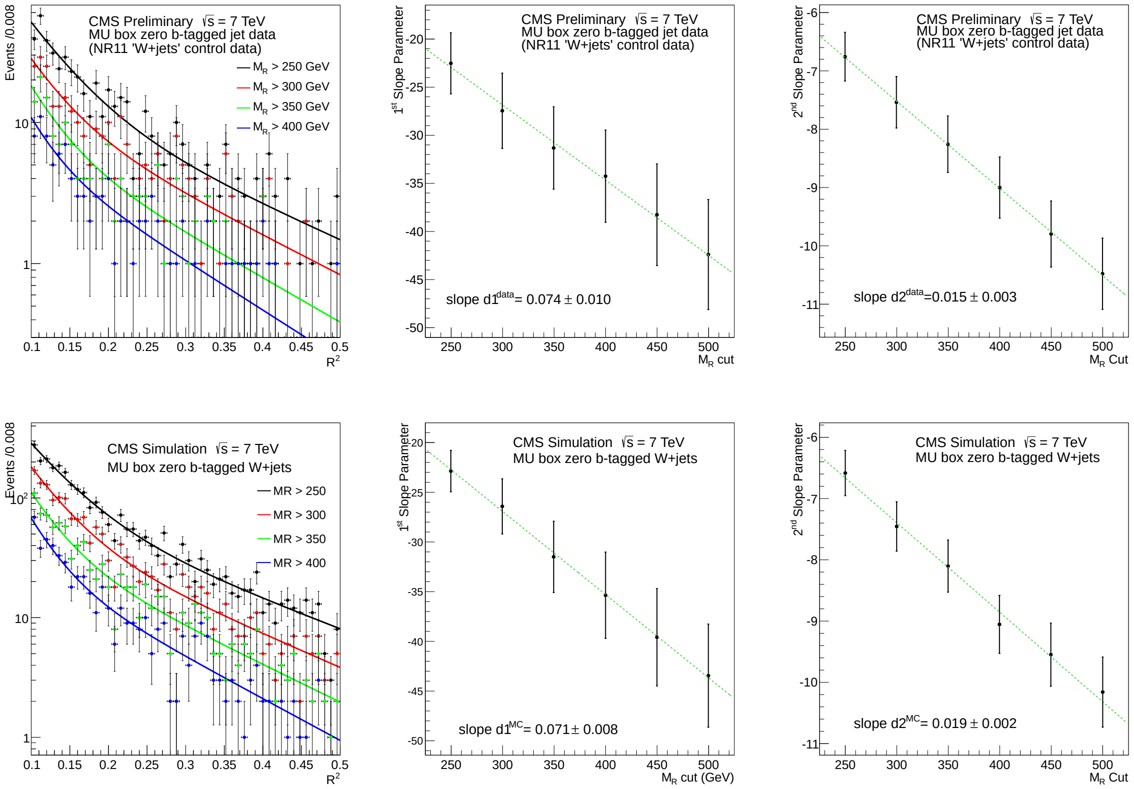

Figure 5: (Top left) R^2 distributions for different values of the M_R threshold for events in data selected in the MU box with the requirement of 0 b-tagged jets. The dotted lines show two independent exponential components fit to the the R^2 distribution, (top center) value of the first exponential slope S from fits to the R^2 distribution, as a function of the M_R threshold (top right) value of the second exponential slope S from fits to the R^2 distribution, as a function of the M_R threshold. (Bottom) The corresponding in simulated W+jets events.

To obtain the initial background shapes we parameterize the pdf of each process by using specific data control samples. For the QCD multijet background we use a set of pre-scaled single-jet triggers for the hadronic box. We invert the isolation (electron id) requirement in order to select a sample of *anti-muon* (*anti-electron*) events from the MU (ELE) box as discussed in detail in [2].

For $t\bar{t}$ we use the NR11 data in the five leptonic and dileptonic boxes, requiring at least one b-tagged jet. This sample is about 90% pure, as estimated from simulation studies. We neglect the residual contamination, mainly due to W+jets events. These $t\bar{t}$ control samples are simultaneously fitted, enforcing the universality of the second component.

The normalization and the second-component fraction f_2 are found to be box specific as expected.

Similarly, we use the NR11 events in the four leptonic and same-flavor dileptonic boxes requiring 0 b-tagged jets to describe the W+jets and Z+jets background. The shape parameters (those of Eq. 16 and 17) are determined for each box through the 2D fit. Gaussian penalty terms are imposed for the parameters k_j, $M^0_{R,j}$ and $R^2_{0,j}$.

The result of the fits to the data control samples are used as initial values for the 2D fits in each of the boxes. The uncertainties on the shape parameters, extracted from the data control sample fits, are used as the σ of the penalty terms multiplying the likelihood.

The values of the shape parameters that maximize the likelihood in these fits, along with the corresponding covariance matrix, are used to define the background model and the uncertainty associated to it.

Once this parameterization is determined, it is used to estimate the total SM background yield in regions where a SUSY or other new physics signal would be visible. In the absence of such a signal, the background shape is used to constrain the parameters of the new physics model under consideration.

We perform the fit to the background shapes in the regions delimited by the green dashed lines in Fig. 8 and Fig. 9. The result of the ML fit projected on M_R and R^2 is shown in Fig. 6 for the dilepton boxes and Fig 7 for the MU, ELE and HAD boxes. No significant discrepancy is observed between the data and the fit model.

It should be noted that the fit cannot resolve the individual background components in the far tail of the distribution, due to the similarity of the shapes of the second components. However the total contribution is well constrained, since the uncertainties on the individual yields cancel out due to the anti-correlation.

9 Definition of Signal Regions

In order to establish the compatibility of the background model to the observed dataset, we define a set of signal regions (SR) on the tail of the background distribution.

The SR are chosen before looking at the data, based on the prediction of the background model obtained by Monte Carlo simulation. The SR are defined such that full range of M_R values (after the event selection) is covered. Different requirements on R^2 are used in different SR, such that the expected background yield is kept small. The defined SR are shown in Fig. 8 (for MU-MU, MU-ELE, and ELE-ELE boxes) and Fig. 9 (for MU, ELE, and HAD).

Using the background model returned by the ML fit, we derive the distribution of the expected yield in each SR using pseudo-experiments.

In order to correctly account for correlations and uncertainties on the parameters describing the background model, the shape parameters used to generate each pseudo-experiment dataset are sampled from the covariance matrix returned by the ML fit. The actual number of events in each dataset is then drawn from a Poisson distribution centered on the yield returned by the covariance-matrix sampling. For each pseudo-experiment dataset, the number of events in the SR is found. For each of the SR, the distribution of the number of events derived by the pseudo-experiments is used to calculate a two-sided p-value, corresponding to the probability of observing an equal or less probable outcome for a counting experiment in each SR. The p-values obtained are quoted in Fig. 8 and Fig. 9. In the same figures, we quote the median and the mode of the yield distribution for each SR, together with the observed yield. A 68% probability interval is also calculated, using the probability associated to each yield outcome as the ordering principle.

No evidence for a deviation is observed, which indicates the compatibility of the background model to the data and the absence of a significant excess from non-SM processes.

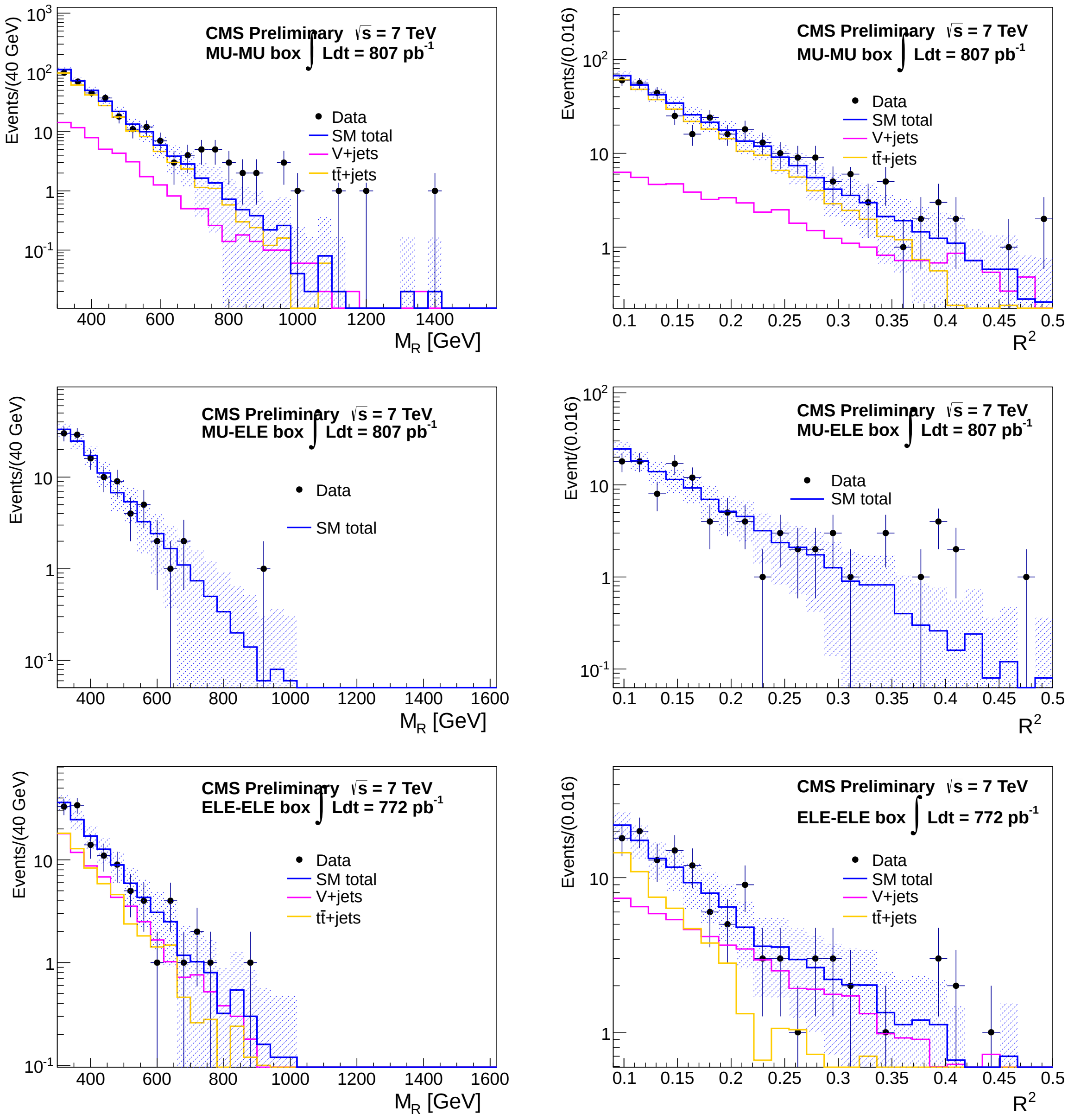

Figure 6: Projection of the 2D fit result on M_R (left) and R^2 (right) for the MU-MU, MU-ELE and ELE-ELE boxes in the YR11 dataset.The blue histogram is the total Standard Model prediction as obtained from a single pseudo-experiment based on the 2D fit. The magenta and yellow histograms show the breakdown of the Standard Model prediction into two separate components as returned by the fit; as verified in simulation, these correspond approximately to the contributions from W,Z + jets and $t\bar{t}$, respectively. The fit is performed in the R^2-M_R sideband and projected into the full region. Only the statistical error on the total SM background prediction is shown. In the MU-ELE box case the total Standard Model background is dominated by the $t\bar{t}$ contribution.

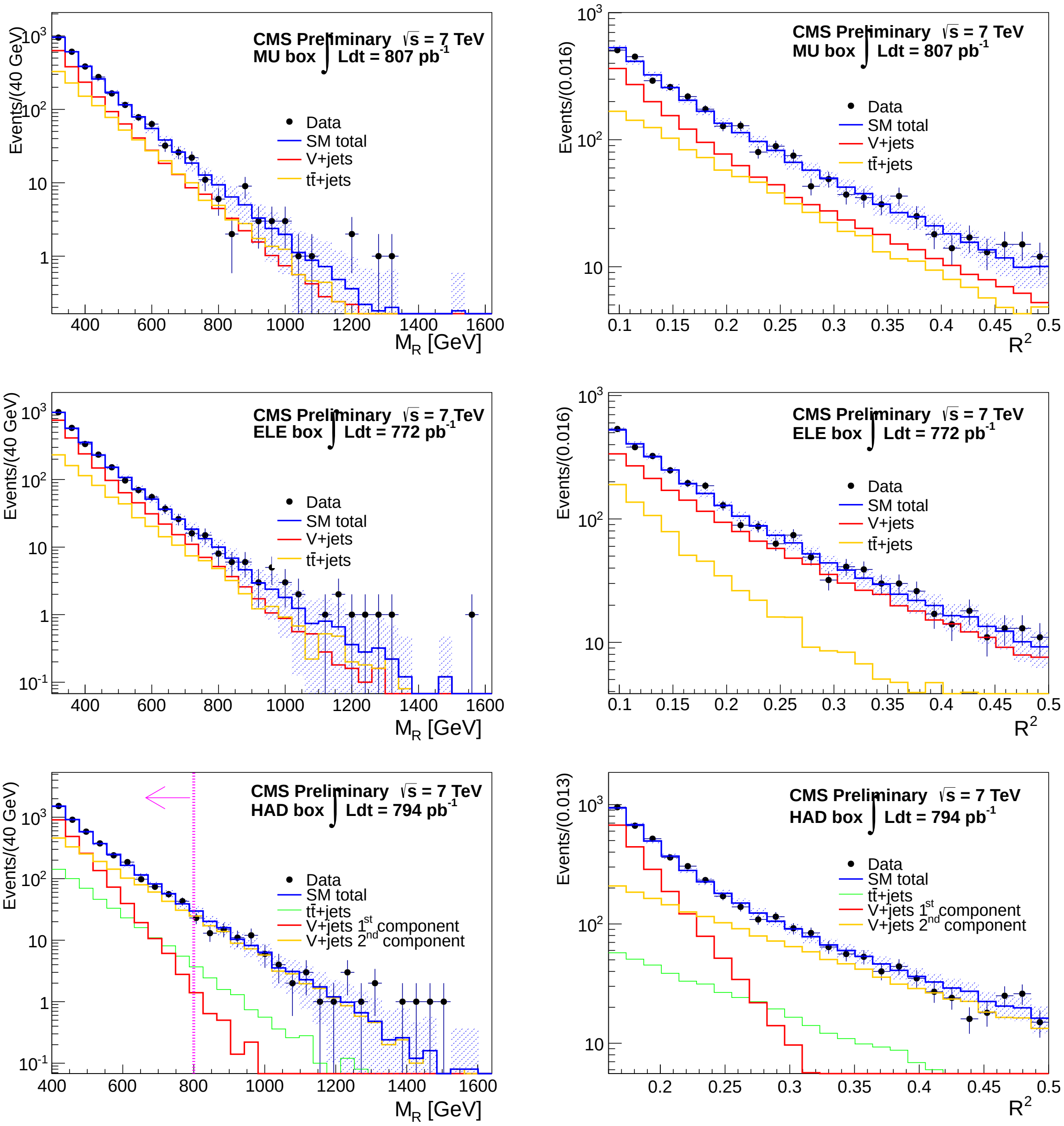

Figure 7: Projection of the 2D fit result on M_R (left) and R^2 (right) for the MU (top), ELE (center), HAD (bottom) boxes in the YR11 dataset. The blue histogram is the total Standard Model prediction as obtained from a single pseudo-experiment based on the 2D fit. The green, red, and yellow histograms show the breakdown of the Standard Model prediction into separate components as returned by the fit; as verified in simulation, these correspond approximately to the contributions from W,Z + jets and $t\bar{t}$. The fit is performed in the R^2-M_R sideband (as an example the magenta dotted line in the HAD box projection on M_R denotes the corresponding fit region) and projected into the full region. Only the statistical error on the total SM background prediction is shown.

10 Interpretation of the Results

We interpret our result as an exclusion limit at 95% confidence level (CL) in the m_0 versus $m_{1/2}$ plane of the CMSSM parameter space for $\tan\beta = 10$, $A_0 = 0$, and positive μ.

We scan the CMSSM parameter space in the the $m_{1/2}$ versus m_0 plane and perform a hypothesis test. There are two well-specified situations under consideration: either the background only hypothesis (H_0) is enough to model the data, or we must include a signal component (H_1) in order to correctly model the distribution seen in data. In the absence of a significant deviation from our background model, we associate a CL to the rejection of H_1 in favor of H_0, computing the value of the hybrid CL_s [13] for that model point.

Each hypothesis is represented as a likelihood function. The hypothesis H_0 is associated to the likelihood function of Eq. 15, while the likelihood function associated to H_1 is written as:

$$\mathcal{L}_{s+b} = \frac{e^{-N_S-(\sum_{j\in SM} N_j)}}{N!} \prod_{i=1}^{N} (N_S P_S(M_{R,i}, R_i^2) + \sum_{j\in SM} N_j P_j(M_{R,i}, R_i^2)) \,, \tag{18}$$

where the background parameters N_j and the pdf's $P_j(M_R, R^2)$ are the same as in Eq. 15; N_S is the expected signal yield, and $P_S(M_R, R^2)$ is the pdf associated to the model-point, parameterized as a 2D template function using Monte Carlo simulation. To avoid effects caused by the finite Monte Carlo statistics of the signal pdfs, we fill the 2D pdf by process (for each of the hadroproduction processes that the analysis is sensitive to) and use the same weighted sum for all the boxes; we assign an additional 20% systematic bin by bin to account for possible shape differences in the different boxes. We use variable binning in M_R to further avoid sparse signal pdfs at larger M_R. The value of N_S in each box is computed from the NLO cross section of the considered model point, the nominal luminosity value corresponding to the dataset, and the reconstruction efficiency for the considered model point, evaluated using Monte Carlo simulation. In leptonic boxes, the shape and normalization of the signal pdf is corrected for the data–simulation agreement on the efficiency of the lepton selection, as determined with a tag-and-probe study performed on a sample of reconstructed $Z \to \ell\ell$ decays ($\ell = e, \mu$) in bins of p_T and η.

For each box we consider the test statistics given by the logarithm of the likelihood ratio $\ln Q = \ln\frac{\mathcal{L}(s+b|H)}{\mathcal{L}(b|H)}$, where H is the hypothesis under test H_1 (signal plus background) or the null hypothesis H_0 (background-only). For a given dataset, we evaluate $\ln Q$ in the full region of events passing the baseline selection, excluding only the events belonging to the *fit region*. These box-specific test statistics are combined in a total discriminant, writing the total likelihood as the product of the likelihoods of each box. This implies that the combined value for $\ln Q$ is given by $\ln Q_{TOT} = \Sigma_{box} \ln Q_{box}$.

Assuming the validity of H_0, the distribution of $\ln Q$ is derived from an ensemble of background-only pseudo-experiments, following the same procedure as described in Sec. 9.

We determine the distribution of $\ln Q$ under the assumption of H_1 by sampling pseudo-experiment datasets out of the likelihood function of Eq. 18. As for the background-only pseudo-experiments, the background model for each generation is derived from the covariance matrix returned by the ML fit. Similarly, the signal pdf is varied *at generation* in each pseudo-experiment, in order to take into account the systematic error associated to the normalization and the shape of the signal distribution. We consider effects across the R^2– M_R plane that coherently affect the overall normalization, as well as systematic effects that vary across the R^2–M_R plane and between final state boxes which can affect the signal pdf shape. Bin-by-bin, the total systematic error on the $P_S(M_R, R^2)$ function of Eq. 18 is the convolution of the individual effects each modeled with a log-normal function. The systematic effects on the signal yield and the the signal shape modeling are summarized in Table 1. We consider variations of the function modeling the signal uncertainty (log-normal vs Gaussian) as well as the binning finding negligible deviations in the result.

While the systematic uncertainties are included when sampling the pseudo-experiments, the likelihood values are computed taking the nominal values for the shape and normalization parameters for both the background and signal pdf's.

Given the distribution of $\ln Q$ for background-only and signal-plus-background pseudo-experiments, the value of $\ln Q$ observed in the data $\ln Q^{\text{data}}$ determines the two tail regions of Fig. 10, the integral of which yields the values of CL_{s+b} and $1 - CL_b$. From these values we compute $CL_s = CL_{s+b}/CL_b$. These CL_s values are used to set a limit in the CMSSM plane, excluding models at 95% CL if $CL_s < 0.05$. The result is shown in Figure 11.

The observed limit is within the ± one standard deviation band of the median expected limit through the (m_0, $m_{1/2}$) plane shown. We note that different regions in the R^2– M_R plane have different sensitivity to different CMSSM models in the (m_0, $m_{1/2}$) plane. In general we are sensitive to squark-squark production at the low m_0–high R^2 regions and gluino-gluino production at higher m_0–lower R^2 regions. The width of the expected limit band changes as a function of the signal production processes in the (m_0, $m_{1/2}$) plane and represents roughly the same range of signal yields throughout the CMSSM plane. The total observed limit is dominated by the HAD box. While the total limit is always better, the difference in the observed total and HAD-only limits cannot be resolved because of the scan granularity in $m_{1/2}$. The two observed limits are drawn identical with an offset representing the hierarchy of the sensitivity. The limit from combining the five lepton boxes limit is also shown. We note that the razor analysis provides the most stringent expected limit for squark and gluino production at the LHC to-date in the CMSSM plane.

Table 1: Summary of the systematic uncertainties on the signal yield and shape.

yield systematics	
$\mathcal{L}$[28]	4.5%
cross section	point-by-point
trigger efficiency R^2-M_R	2%
trigger efficiency lepton	3% (lepton, dilepton boxes)
shape systematics	
2D signal shape	20% (bin-by-bin)
PDF	point-by-point (up to 30%)
JES	point-by-point (up to 1%)
lepton-id (tag-and-probe)	1% (per lepton)

11 Summary

We performed a search for squarks and gluinos using a data sample of $\sim$800 pb^{-1} integrated luminosity from pp collisions at $\sqrt{s} = 7$ TeV, recorded by the CMS detector at the LHC. The kinematic consistency of the selected events was tested against the hypothesis of heavy particle pair production using the dimensionless razor variable R related to the missing transverse energy $E_{\mathrm{T}}^{\text{miss}}$, and M_R, an event-by-event indicator of the heavy particle mass scale. In a control dataset we find a simple functional form that describes the distributions of the relevant SM backgrounds as a function of R^2 and M_R. This functional form is used to perform a 2D fit of the SM backgrounds, based on which we predict the background yields and shapes in regions at high mass scale that could contain events from new physics.

No significant excess over the background expectations was observed and the results were presented as a 95% CL in the (m_0, $m_{1/2}$) CMSSM parameter space. These results significantly extend the current LHC limits at m_0 values above 800 GeV.

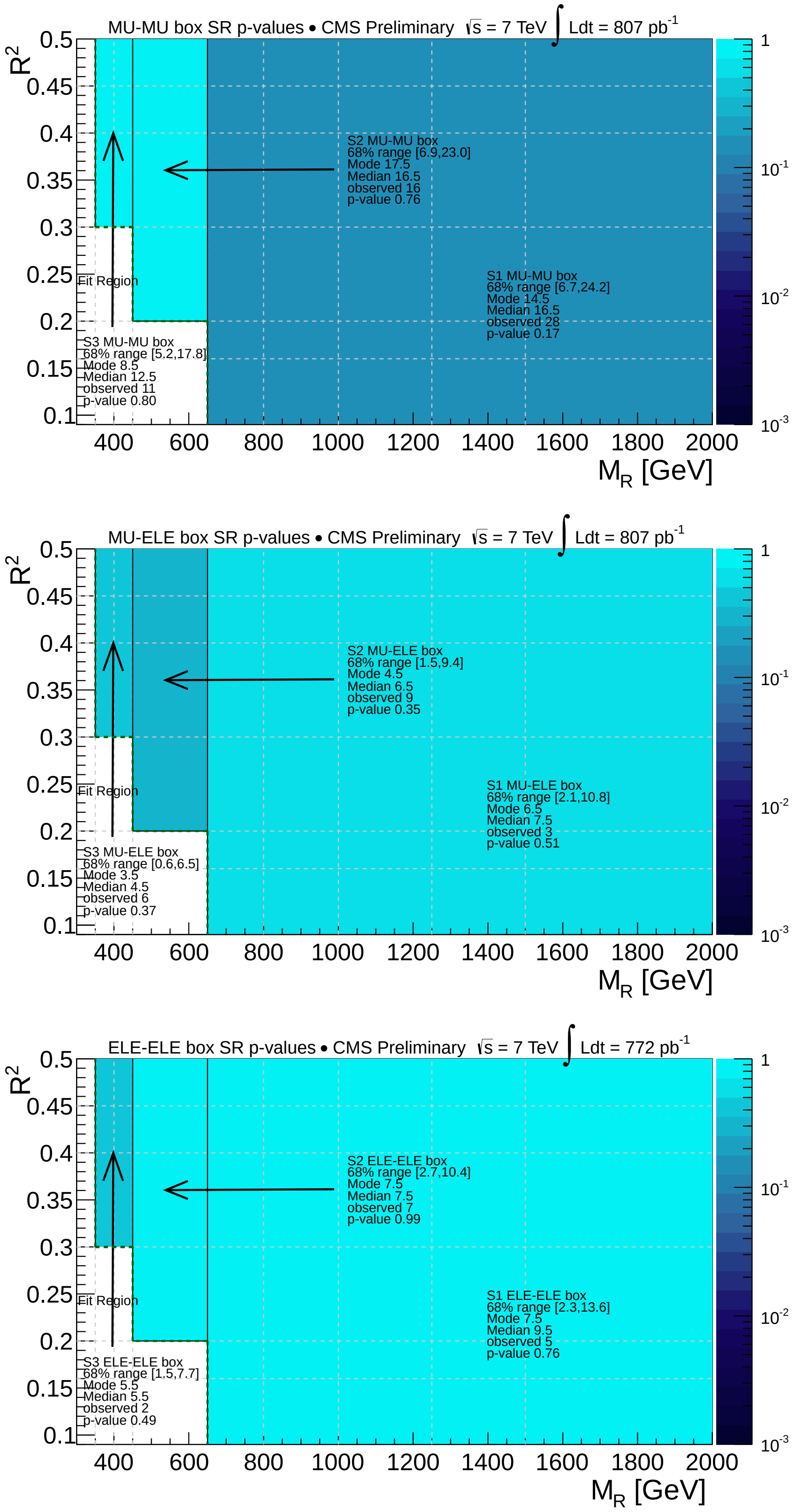

Figure 8: The p-values corresponding to the observed number of events in the MU-MU (top), MU-ELE (center), and ELE-ELE (bottom) box signal regions defined for this analysis. The green dotted lines indicate the fit regions. The p-values test the compatibility of the observed number of events in data with the SM expectation (obtained from the background parameterization).

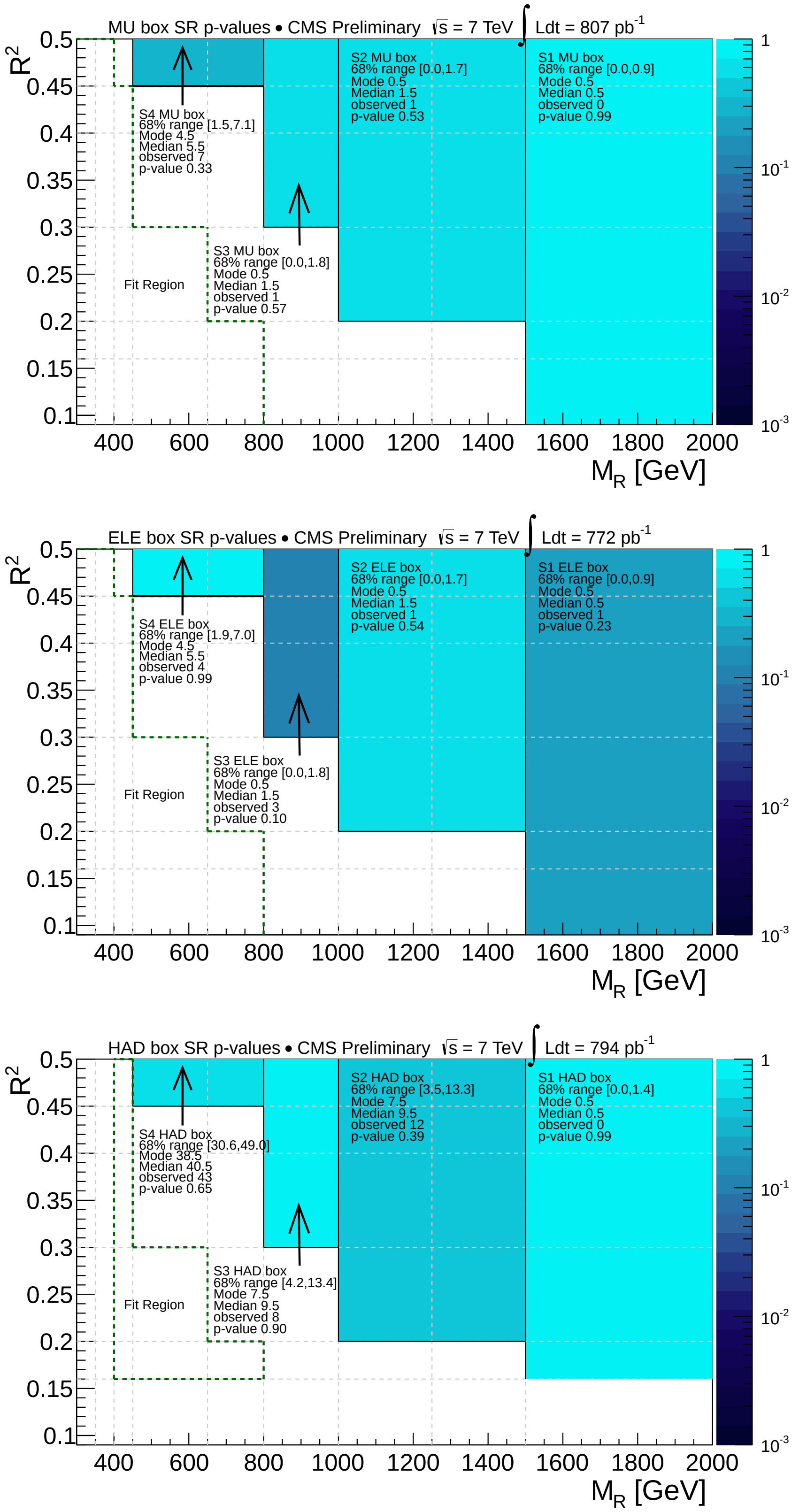

Figure 9: The p-values corresponding to the observed number of events in the MU (top), ELE (middle), and HAD (bottom) box signal regions defined for this analysis. The green dotted lines indicate the fit regions. The p-values test the compatibility of the observed number of events in data with the SM expectation (obtained from the background parameterization).

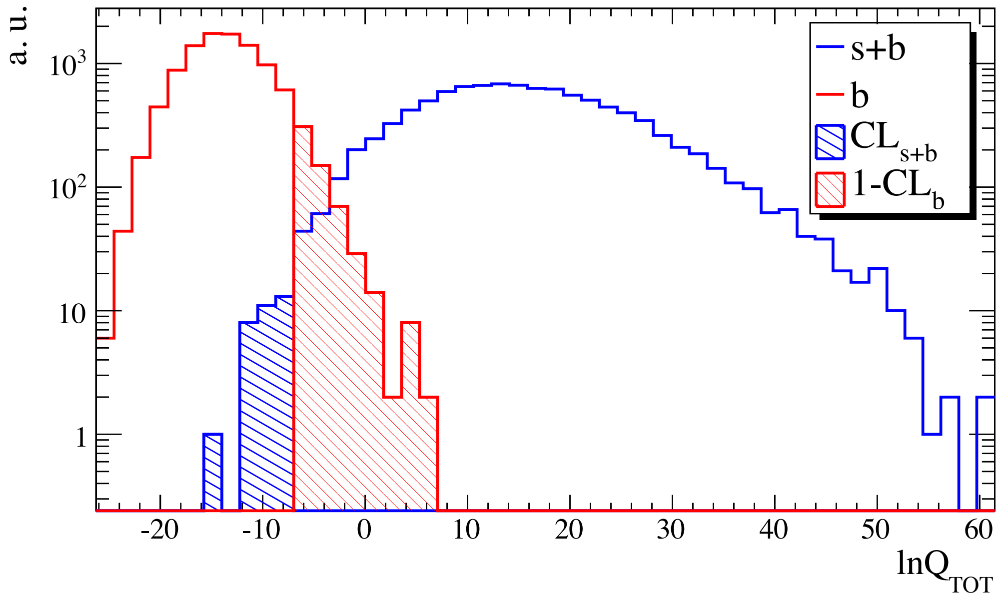

Figure 10: Distribution of $\ln Q_{TOT}$ for background-only (left) and signal+background (right) pseudo-experiments, corresponding to a CMSSM model with $A_0 = 0$, positive sign of μ, $\tan\beta = 10$, $m_0 = 1000$ GeV, and $m_{1/2} = 305$ GeV. Here, the subscript TOT indicates that all six final state boxes are used in constructing the test statistic. The value $\ln Q_{TOT}^{\text{data}} = -8.55$ observed on data delimits the CL_s and $1 - CL_b$ tails, shown as hatched regions in the figure.

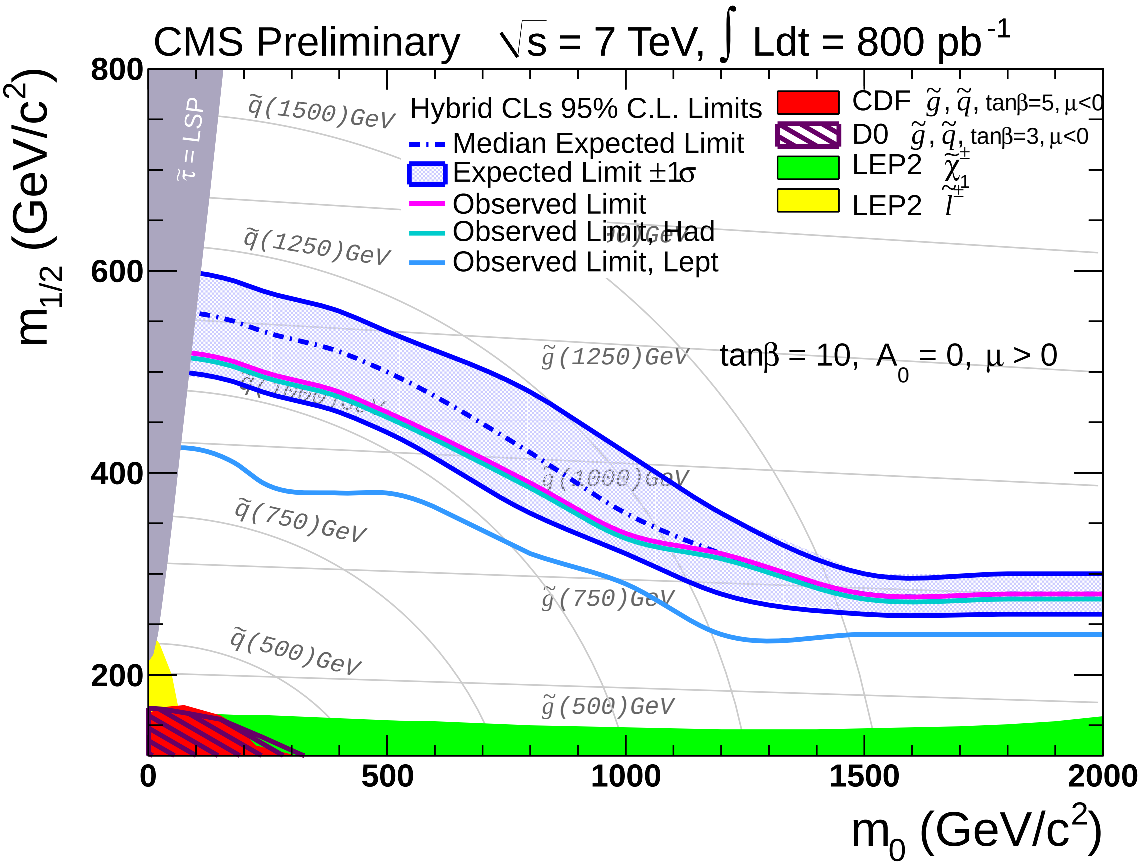

Figure 11: Observed (solid magenta curve) and median expected (dot-dashed blue curve) 95% CL limits in the $(m_0, m_{1/2})$ CMSSM plane with $\tan\beta = 10$, $A_0 = 0$, $\mathrm{sgn}(\mu) = +1$ from the razor analysis. The ± one standard deviation equivalent variations in the uncertainties are shown as a band around the median expected limit. In solid cyan the observed HAD box limit, and in solid light-blue the observed limit from combining the lepton boxes, are also shown. The EWKB region is not shown.

References

[1] C. Rogan, "Kinematics for new dynamics at the LHC", `arXiv:1006.2727`. CALT-68-2790.

[2] CMS Collaboration, "Inclusive search for squarks and gluinos in pp collisions at sqrt(s) = 7 TeV", `arXiv:1107.1279`.

[3] D0 Collaboration, "Search for squarks and gluinos in events with jets and missing transverse energy using 2.1 fb^{-1} of p anti-p collision data at s$^{(1/2)}$ = 1.96 TeV", *Phys. Lett.* **B660** (2008) 449–457, `arXiv:0712.3805`. `doi:10.1016/j.physletb.2008.01.042`.

[4] CDF Collaboration, "Inclusive Search for Squark and Gluino Production in p anti-p Collisions at s$^{(1/2)}$ = 1.96 TeV", *Phys. Rev. Lett.* **102** (2009) 121801, `arXiv:0811.2512`. `doi:10.1103/PhysRevLett.102.121801`.

[5] Atlas Collaboration, "Search for squarks and gluinos using final states with jets and missing transverse momentum with the ATLAS detector in sqrt(s) = 7 TeV proton-proton collisions", `arXiv:1102.5290`.

[6] Atlas Collaboration, "Search for supersymmetry using final states with one lepton, jets, and missing transverse momentum with the ATLAS detector in sqrt(s) = 7 TeV pp", `arXiv:1102.2357`.

[7] CMS Collaboration, "Search for new physics with the jets and missing momentum signature at the LHC", *CMS PAS* **SUS-10-005** (2011).

[8] CMS Collaboration, "Search for Supersymmetry in pp Collisions at 7 TeV in Events with Jets and Missing Transverse Energy", *Phys. Lett.* **B698** (2011) 196–218, `arXiv:1101.1628`. `doi:10.1016/j.physletb.2011.03.021`.

[9] CMS Collaboration, "Search for new physics with same-sign isolated dilepton events with jets and missing transverse energy at the LHC", `arXiv:1104.3168`.

[10] CMS Collaboration, "Search for Physics Beyond the Standard Model in Opposite- Sign Dilepton Events at sqrt(s) = 7 TeV", `arXiv:1103.1348`.

[11] CMS Collaboration, "The CMS experiment at the CERN LHC", *JINST* **3** (2008) S08004. `doi:10.1088/1748-0221/3/08/S08004`.

[12] CMS Collaboration, "CMS technical design report, volume II: Physics performance", *J. Phys. G* **34** (2007) 995–1579. `doi:10.1088/0954-3899/34/6/S01`.

[13] A. L. Read, "Presentation of search results: The CL(s) technique", *J.Phys.G* **G28** (2002) 2693–2704. `doi:10.1088/0954-3899/28/10/313`.

[14] T. Sjöstrand, S. Mrenna, and P. Skands, "PYTHIA 6.4 Physics and Manual; v6.420, tune D6T", *JHEP* **05** (2006) 026, `arXiv:hep-ph/0603175`.

[15] F. Maltoni and T. Stelzer, "MadEvent: Automatic event generation with MadGraph", *JHEP* **02** (2003) 027, `arXiv:hep-ph/0208156`.

[16] GEANT4 Collaboration, "GEANT4: A simulation toolkit", *Nucl. Instrum. Meth.* **A506** (2003) 250–303. `doi:10.1016/S0168-9002(03)01368-8`.

[17] B. C. Allanach, “SOFTSUSY: a program for calculating supersymmetric spectra”, *Comput. Phys. Commun.* **143** (2002) 305–331, `arXiv:hep-ph/0104145`. `doi:10.1016/S0010-4655(01)00460-X`.

[18] A. Djouadi, M. M. Muhlleitner, and M. Spira, “Decays of Supersymmetric Particles: the program SUSY-HIT (SUspect-SdecaY-Hdecay-InTerface)”, *Acta Phys. Polon.* **B38** (2007) 635–644, `arXiv:hep-ph/0609292`.

[19] P. Z. Skands et al., “SUSY Les Houches Accord: Interfacing SUSY Spectrum Calculators, Decay Packages, and Event Generators”, *JHEP* **07** (2004) 036, `arXiv:hep-ph/0311123`. `doi:10.1088/1126-6708/2004/07/036`.

[20] W. Beenakker, R. Hopker, and M. Spira, “PROSPINO: A program for the PROduction of Supersymmetric Particles In Next-to-leading Order QCD”, `arXiv:hep-ph/9611232`.

[21] CMS Collaboration, “Tracking and Primary Vertex Results in First 7 TeV Collisions”, *CMS PAS* **TRK-10-005** (2010).

[22] M. Cacciari, G. P. Salam, and G. Soyez, “The anti-kt jet clustering algorithm”, *JHEP* **0804** (2008) 063–074. `doi:10.1088/1126-6708/2008/04/063`.

[23] CMS Collaboration, “Determination of the Jet Energy Scale in CMS with pp Collisions at sqrt(s) = 7 TeV”, *CMS PAS* **JME-10-010** (2010).

[24] CMS Collaboration, “Commissioning of the Particle-Flow Reconstruction in Minimum-Bias and Jet Events from pp Collisions at 7 TeV”, *CMS PAS* **PFT-10-002** (2010).

[25] CMS Collaboration, “Measurements of Inclusive W and Z Cross Sections in pp Collisions at 7 TeV”, *CMS PAS* **EWK-10-002** (2010).

[26] W. Verkerke and D. P. Kirkby, “The RooFit toolkit for data modeling”, `arXiv:physics/0306116`.

[27] R. J. Barlow, “Extended maximum likelihood”, *Nucl.Instrum.Meth.* **A297** (1990) 496–506. `doi:10.1016/0168-9002(90)91334-8`.

[28] CMS Collaboration, “Absolute luminosity normalization”, *CMS DPS* **CERN-CMS-DP-2011-002** (2011).